aerospace

MDPI

Article

Localized Plateau-Based Validation of Classical Phenomenological Models for Superelastic Shape Memory Alloys

Saeed Danaee Barforooshi, Girolamo Costanza * and Maria Elisa Tata

Industrial Engineering Department, University of Rome Tor Vergata, 00133 Rome, Italy; saeed.danaeebarforooshi@alumni.uniroma.eu (S.D.B.); elisa.tata@uniroma2.it (M.E.T.)
* Correspondence: costanza@ing.uniroma2.it

Abstract

The superelastic behavior of shape memory alloys (SMAs) arises from stress-induced martensitic transformation and plays an important role in the design of smart engineering systems, including aerospace components. Reliable constitutive modeling is therefore essential for accurately predicting their mechanical response in numerical simulations of SMA-based engineering systems. In this study, a localized plateau-based comparative evaluation framework is employed to compare the classical Brinson and Liang–Rogers phenomenological models using published experimental stress–strain data of superelastic NiTi alloys under isothermal tensile loading–unloading conditions at two different temperatures. Model performance is assessed using global RMSE, localized plateau RMSE, and hysteretic energy dissipation. The results show that both constitutive models provide close agreement with the overall superelastic hysteresis response and predict comparable hysteretic energy dissipation. However, the Liang–Rogers model consistently provides lower localized RMSE values within the forward and reverse transformation plateau regions. The principal contribution of this work is the introduction of a localized comparative evaluation framework that complements conventional global error measures for comparing phenomenological SMA constitutive models.

Keywords: shape memory alloys; phenomenological models; superelastic; localized plateau-based evaluation

1. Introduction

Shape memory alloys (SMAs) are smart materials that can recover large inelastic strains through a reversible martensite transformation. Nickel–titanium (NiTi) alloy, which is nearly equiatomic, has attracted considerable attention owing to its excellent superelastic performance, high strain recovery, corrosion resistance, and high energy absorption capacity. Due to such properties, SMAs find application in biomedical devices, aerospace components, robotics, vibration isolation, and adaptive engineering systems [1–4]. In aerospace engineering, superelastic NiTi SMAs have been increasingly adopted for morphing wings, adaptive airfoils, deployable space structures, vibration suppression devices, and lightweight smart actuators because of their high actuation capability, compactness, and favorable strength-to-weight ratio [5–7]. Accurate constitutive modeling of superelastic SMAs is essential for the numerical simulation and design of advanced engineering systems, including aerospace structures and smart components, where reliable prediction of stress-induced transformation behavior is required.

Check for updates

Academic Editor: Mostafa El Sayed

Received: 24 June 2026
Revised: 4 September 2026
Accepted: 6 September 2026
Published: 7 September 2026

Copyright: © 2026 by the authors. Licensee MDPI, Basel, Switzerland. This article is an open access article distributed under the terms and conditions of the Creative Commons Attribution (CC BY) license.

The macroscale properties of SMAs originate from the reversible phase transition of austenite to martensite and vice versa when subjected to thermal and/or mechanical loads. If the material is stressed at temperatures higher than the austenite finish temperature, a stress-induced phase transformation of martensite occurs, resulting in a superelastic hysteresis loop, which involves loading and unloading plateaus along with substantial strain recovery. Therefore, accurate constitutive models are essential for the reliable numerical simulation and design of SMA-based engineering systems [8–10].

Over the years, many constitutive equations have been developed to model the thermomechanical behavior of shape memory alloys. They can be classified into micromechanical models, thermodynamic models, and phenomenological models [9–25]. Among these, phenomenological constitutive models are more commonly used because of their mathematical simplicity, low computational cost, and reasonable accuracy in reproducing the hysteretic behavior of SMAs. Accordingly, the present study focuses on two representative and historically influential formulations, namely, the Liang–Rogers and Brinson models, which have served as the foundation for many subsequent constitutive developments.

One-dimensional phenomenological constitutive models have provided the foundation for many subsequent SMA constitutive theories [26]. The early phenomenological models proposed by Tanaka [20] and later extended by Liang and Rogers [19] describe the constitutive response using the evolution of the martensitic volume fraction during stress-induced phase transformation. The Liang–Rogers theory improves the description of the transformation process through the definition of distinct transformation stress intervals during loading and unloading. Further advancements in these models are associated with the separation of stress-induced and temperature-induced martensitic fractions.

However, most comparative studies have primarily focused on reproducing the overall hysteresis response or evaluating global prediction errors, whereas considerably less attention has been devoted to the localized analysis of the transformation regions [27,28]. Moreover, the consistency of comparative trends under different testing temperatures has received limited attention. The aim of the present study is to compare the Brinson and Liang–Rogers phenomenological constitutive models for the superelastic behavior of NiTi SMAs under isothermal loading using a plateau-based comparative evaluation framework. The comparison is performed through global RMSE analysis, localized transformation plateau evaluation, and hysteretic energy dissipation. Such a comparative assessment provides guidance for selecting constitutive models in numerical simulations of SMA-based smart structures and actuators, particularly in aerospace applications where the accurate prediction of phase transformation behavior is essential.

2. Materials and Methods

2.1. Experimental Dataset

The experimental datasets used for comparative evaluation were adopted from the work of Zidane and Meddour [29], whose numerical study employed the experimental tensile data originally reported by Ng and Sun [30] for superelastic NiTi shape memory alloy. Two experimental datasets corresponding to isothermal tensile loading–unloading tests performed at 65 °C and 70 °C were selected for the present comparative study. These datasets provide complete superelastic stress–strain responses under identical loading conditions but at different temperatures.

Because the objective of the present work is to compare the performance of two classical phenomenological constitutive models under identical experimental conditions, no additional experiments were conducted. Instead, both constitutive models were evaluated using the same published experimental datasets to ensure a consistent comparative assessment. It should be noted that the two datasets arise from the same experimental source

and therefore represent two comparative test cases at different temperatures rather than two independent experimental campaigns.

2.2. Material Parameters

The material parameters employed in the present study are summarized in Table 1. The elastic moduli and transformation strain were kept identical for the two test cases, whereas the transformation stress limits were specified separately for each test temperature. The parameter values were adopted from the experimental characterization and temperature-dependent transformation data reported by Zidane and Meddour [29], based on the experimental NiTi stress–strain data originally reported by Ng and Sun [30]. Accordingly, the values of σ_{MS}, σ_{MF}, σ_{AS}, and σ_{AF} used for Tests 1 and 2 correspond to the respective 65 °C and 70 °C experimental conditions. No recalibration or parameter optimization was performed in the present work.

Table 1. Material parameters and their values.

Parameter	Test 1 (65 °C)	Test 2 (70 °C)
E_A	25,775 MPa	25,775 MPa
E_M	18,442 MPa	18,442 MPa
ε_L	0.06	0.06
σ_{MS}	268 MPa	279 MPa
σ_{MF}	275 MPa	306 MPa
σ_{AS}	62 MPa	83 MPa
σ_{AF}	37 MPa	60 MPa

2.3. Constitutive Modeling

The superelastic behavior of SMAs in uniaxial stress conditions is often expressed using one-dimensional phenomenological models, where the macroscale deformation is controlled by the development of an internal variable related to phase transition, usually the volume fraction of martensite.

The total strain ε is decomposed into an elastic part and a transformation-induced part:

$$\varepsilon = \varepsilon^e + \varepsilon^{tr} \tag{1}$$

where the transformation strain is assumed proportional to the martensite fraction,

$$\varepsilon^{tr} = \varepsilon_L \xi \tag{2}$$

and ε_L is the maximum transformation strain.

The stress–strain relation is expressed as:

$$\sigma = E(\xi)(\varepsilon - \varepsilon_L \xi) \tag{3}$$

For the Brinson formulation, the effective elastic modulus is taken as a function of the martensite fraction according to the rule of mixtures,

$$E(\xi) = E_A(1 - \xi) + E_M \xi \tag{4}$$

whereas E_A and E_M stand for Young's moduli of the austenitic and martensitic phases, respectively. This martensite-fraction-dependent treatment of the elastic modulus is specific to the Brinson formulation considered in the present study. By contrast, the Liang–Rogers formulation treats the elastic modulus as a constant material property and does not introduce a dependence on the martensite fraction.

The Brinson and Liang–Rogers models were selected because both are representative classical phenomenological formulations for modeling the superelastic response of SMAs under isothermal loading. Both formulations describe stress-induced martensitic transformation through the evolution of a martensite-related internal variable and employ cosine-based transformation relations in the present implementation. However, they differ in their treatment of the constitutive response: the Brinson formulation incorporates a martensite-fraction-dependent elastic modulus, whereas the Liang–Rogers formulation treats the elastic modulus as a constant material property. These differences can lead to different stress predictions within the transformation regions.

2.3.1. Brinson Model

The Brinson model [17] extends earlier phenomenological SMA models by incorporating the evolution of the martensitic volume fraction to provide a smooth representation of the stress-induced phase transformation. Under isothermal loading conditions, the model describes the transformation as a continuous process driven by the applied stress.

The Brinson model separates the martensite fraction into stress-induced and temperature-induced components, i.e.,

$$\xi = \xi_S + \xi_T \tag{5}$$

where ξ_S and ξ_T denote the stress-induced and temperature-induced martensite fractions, respectively. Because the present comparative test cases are performed under isothermal mechanical loading at constant temperature, no temperature-induced evolution of the martensite fraction occurs during the loading–unloading cycle. Therefore, $\xi_T = 0$ for the present simulations, and Equation (5) reduces to $\xi = \xi_S$.

For the isothermal conditions considered here, the stress-induced martensitic fraction is therefore the active internal variable. The Brinson formulation additionally accounts for the dependence of the elastic modulus on the current martensite fraction, as specified by Equation (4).

The stress-induced phase transformation is described by cosine-based evolution relations for the forward and reverse transformation branches, as follows:

$$\xi = \begin{cases} 1 - \frac{1-\xi_0}{2}\left[1 + cos\left(\pi \frac{\sigma - \sigma_{MS}}{\sigma_{MF} - \sigma_{MS}}\right)\right], & \sigma_{MS} \le \sigma \le \sigma_{MF} \\ \frac{\xi_0}{2}\left[1 + cos\left(\pi \frac{\sigma - \sigma_{AF}}{\sigma_{AS} - \sigma_{AF}}\right)\right], & \sigma_{AF} \le \sigma \le \sigma_{AS} \end{cases} \tag{6}$$

Here, ξ_0 denotes the initial martensite fraction, while σ_{MS} and σ_{MF} denote the start and finish stresses of the forward transformation, respectively, and σ_{AS} and σ_{AF} denote the start and finish stresses of the reverse transformation, respectively.

The formulation used in the present study represents an isothermal specialization of the general Brinson model. In the general formulation, the total martensite fraction consists of temperature-induced and stress-induced contributions, and the temperature-induced contribution evolves when the temperature changes. Because the present simulations are performed at constant temperatures, the temperature-induced martensite fraction remains constant throughout each loading–unloading cycle. The martensite-fraction evolution considered in the present implementation is therefore governed by the stress-induced transformation component, while the temperature-dependent evolution of the martensite fraction is not activated. This simplification is consistent with the isothermal stress–strain comparison performed in the present study and defines the scope of the Brinson formulation considered here.

2.3.2. Liang–Rogers Model

The Liang–Rogers model [19] describes the stress-induced phase transformation through distinct transformation-stress intervals and the corresponding evolution of the martensitic volume fraction. Under the isothermal conditions considered in the present study, the temperature-dependent terms of the general thermomechanical formulation do not contribute to the mechanical stress–strain response. The martensite fraction therefore evolves according to the following stress-based relations.

For forward transformation:

$$\xi = \frac{1}{2}\left[1 - cos\left(\pi \frac{\sigma - \sigma_{MS}}{\sigma_{MF} - \sigma_{MS}}\right)\right] \tag{7}$$

For reverse transformation:

$$\xi = \frac{1}{2}\left[1 + cos\left(\pi \frac{\sigma - \sigma_{AF}}{\sigma_{AS} - \sigma_{AF}}\right)\right] \tag{8}$$

In this study, this constitutive formulation is implemented numerically through the implicit solution of the constitutive equation to ensure consistency between the stress–strain state and martensite volume fraction.

A key constitutive distinction between the two formulations considered in this study concerns the treatment of the elastic modulus. In the Brinson formulation, the effective modulus varies with the martensite fraction according to Equation (4). In the present Liang–Rogers implementation, the elastic modulus is treated as a constant material property and is taken as the austenitic Young's modulus. This choice is consistent with the initial fully austenitic state of the NiTi specimens at the investigated temperatures of 65 °C and 70 °C. Accordingly, the elastic modulus is not updated as a function of the martensite fraction in the present Liang–Rogers implementation. Thus, although both formulations employ cosine-based relations for the evolution of the martensitic fraction under the present isothermal conditions, their constitutive treatment of the elastic response is different.

For clarity, the main constitutive features of the Brinson and Liang–Rogers formulations as implemented under the isothermal conditions considered in this study are summarized in Table 2. The table highlights the differences in the martensite-related internal variables, initialization, transformation evolution rules, transformation stress intervals, elastic modulus treatment, and loading–unloading branches.

Table 2. Comparison of the Brinson and Liang–Rogers constitutive formulations used in the present study under isothermal superelastic loading–unloading conditions.

Feature	Brinson Model	Liang–Rogers Model
Formulation Scope	General formulation; specialized to isothermal mechanical loading in the present study	Isothermal formulation used for mechanical loading–unloading
Evolution rules	Equation (6)	Equations (7) and (8)
Elastic modulus	Effective modulus depends on martensite fraction	Constant elastic modulus
Transformation conditions	$\sigma_{MF} \geq \sigma \geq \sigma_{MS}$ $\sigma_{AS} \geq \sigma \geq \sigma_{AF}$	Same transformation stress intervals
Martensite fraction	$\xi = \xi_S + \xi_T, \xi_S, \xi_T$	ξ
Initialization	$\xi_{S,0} = 0, \xi_{T,0} = 0$	$\xi_0 = 0$
Loading/unloading logic	Forward transformation during loading; reverse transformation during unloading	Same logic

2.4. Numerical Implementation

The constitutive models were implemented in MATLAB R2022b using an incremental time-stepping procedure under isothermal loading–unloading conditions. A monotonic tensile loading history was prescribed by applying a constant strain rate until the maximum strain was reached, followed by unloading at the same rate. The imposed strain rate was 5.6×10^{-5} s^{-1}. The strain was increased linearly to a maximum value of 7% and subsequently decreased to the initial value at the same strain rate, which defined the complete loading–unloading history. The corresponding loading and unloading durations were 1250 s each.

The simulations were performed using a constant time increment of 0.02 s. The numerical sensitivity to the selected time increment was assessed by repeating the calculation with time steps of 0.04, 0.02, 0.01, and 0.005 s. The global RMSE showed negligible variation as the time step was progressively reduced. In the sensitivity assessment, the Brinson-model RMSE changed from 25.41565 MPa at $\Delta t = 0.04$ s to 25.41559 MPa at $\Delta t = 0.005$ s, whereas the corresponding Liang–Rogers RMSE remained 23.89089 MPa at both time steps. For the selected time step of $\Delta t = 0.02$ s, the relative change in RMSE with respect to the finest time step was approximately 0.00024% for the Brinson model and 0% for the Liang–Rogers model, confirming that the adopted time increment provides a numerically stable and sufficiently converged solution. At each increment, the martensite fraction was updated according to the governing transformation relations of the corresponding model. For the Brinson formulation, the elastic modulus was updated as a function of the current martensite fraction according to Equation (4). For the Liang–Rogers formulation, the elastic modulus was treated as a constant material property throughout the simulation. The corresponding stress response was then evaluated using the constitutive relation of each model.

The same experimental loading history and numerical discretization were adopted for both models to ensure a consistent comparison, while each model retained its respective constitutive treatment of the elastic modulus and martensite evolution.

The loading and unloading branches were identified from the prescribed strain increment. A non-negative strain increment defined the loading branch, whereas a negative strain increment defined the unloading branch. During loading, the forward transformation was activated when the calculated stress entered the transformation interval between the martensite-start and martensite-finish stresses, σ_{MS} and σ_{MF}, respectively. During unloading, the reverse transformation was activated when the stress entered the interval between the austenite-start and austenite-finish stresses, σ_{AS} and σ_{AF}, respectively. Outside the corresponding transformation intervals, the martensite fraction was kept at its current value. The martensite fraction was constrained to the physically admissible range $0 \leq \xi \leq 1$. Accordingly, it was set to $\xi = 1$ after completion of the forward transformation and to $\xi = 0$ after completion of the reverse transformation.

For the Liang–Rogers formulation, the martensite fraction within the transformation intervals was obtained by solving the nonlinear constitutive equation implicitly at each strain increment. The scalar residual for the forward transformation was defined as the difference between the constitutive stress and the stress prescribed by the linear transformation stress relation between σ_{MS} and σ_{MF}. For the reverse transformation, the residual was defined analogously using the transformation stress relation between σ_{AF} and σ_{AS}. The nonlinear equation was solved using MATLAB's fzero root-finding algorithm. For forward transformation, the root was searched within the physically admissible interval $[\xi_{\text{old}}, 1]$, whereas for reverse transformation, the search interval was $[0, \xi_{\text{old}}]$, where ξ_{old} denotes the martensite fraction from the preceding increment. If a valid sign-changing bracket was not obtained, the martensite fraction was retained at its previous value.

The fzero solver was used with its MATLAB default convergence settings. No user-defined iteration limit, function value tolerance, or maximum iteration count was imposed. The solution was therefore accepted according to the default convergence criteria of the MATLAB fzero implementation.

For the two test temperatures, the elastic and transformation strain parameters were kept consistent with the adopted material characterization, whereas the critical transformation stress limits were specified according to the corresponding test temperature. Accordingly, temperature-specific transformation stress values were used for two cases to account for the experimentally observed temperature dependence of the transformation stresses.

The simulated stress–strain curves were compared with the experimental datasets by linearly interpolating the numerical results at the experimental strain points. A total of 157 and 170 experimental stress–strain data points were used for Test 1 and Test 2, respectively. The published experimental stress–strain curves were converted into numerical data points for quantitative comparison, and the extracted data were subsequently interpolated consistently for the RMSE calculations. The global root-mean-square error (RMSE), localized plateau RMSE, and hysteretic energy dissipation were subsequently calculated as quantitative performance indicators.

2.5. Model Evaluation Metrics

2.5.1. Global RMSE

The agreement of each constitutive model with the experimental stress–strain data was first evaluated using the global RMSE, which measures the overall agreement between the numerical predictions and the experimental stress–strain data over the complete loading–unloading cycle. The RMSE was calculated as:

$$RMSE = \sqrt{\frac{1}{N}\sum\left(\sigma_i^{num} - \sigma_i^{exp}\right)^2} \tag{9}$$

where N denotes the number of experimental data points, while σ_i^{num} and σ_i^{exp} represent the numerical and experimental stresses, respectively.

2.5.2. Localized Plateau Analysis

Because the stress-induced martensitic transformation mainly occurs within the loading and unloading plateaus, a localized plateau analysis was additionally performed. The forward and reverse transformation regions were treated separately using fixed numerical stress intervals defined for each experimental test. The plateau intervals were defined as fixed numerical stress windows based on the experimentally observed transformation-stress levels and the corresponding low-slope transformation regions. Once the stress intervals were specified, the experimental data point selection was performed using the explicit criterion $\sigma_{\min} \leq \sigma_{\exp} \leq \sigma_{\max}$, where $\sigma_{\min}$ and $\sigma_{\max}$ denote the lower and upper bounds of the predefined plateau interval, respectively. Thus, the experimental points included in the localized RMSE calculation are determined solely by their measured stress and the predefined numerical bounds, independently of the predictions of either constitutive model. The same stress intervals were then applied to both constitutive models to ensure a consistent comparison.

The localized RMSE was then calculated only over the experimental points satisfying this criterion, according to:

$$RMSE_{Plateau} = \sqrt{\frac{1}{M}\sum\left(\sigma_i^{num} - \sigma_i^{exp}\right)^2} \tag{10}$$

For Test 1 at 65 °C, the upper and lower plateau intervals were defined as 260–285 MPa and 30–60 MPa, respectively, whereas for Test 2 at 70 °C, the corresponding intervals were 270–310 MPa and 45–90 MPa. The strain ranges and numbers of retained experimental data points within these intervals are reported in Table 3.

Table 3. Definition of the localized transformation plateau regions and retained experimental data points.

Test	Branch	Plateau	Stress Interval (MPa)	Retained Experimental Strain Range (%)	No. of Retained Experimental Points
Test 1	Loading	Upper	260–285	1.012–6.657	44
Test 1	Unloading	Lower	30–60	0.305–5.806	62
Test 2	Loading	Upper	270–310	1.059–7.152	55
Test 2	Unloading	Lower	45–90	0.434–5.621	44

To assess the robustness of the localized comparison to the selected plateau boundaries, the baseline stress intervals were perturbed by ±5 MPa at both boundaries. Narrowed, baseline, and widened intervals were considered, and the localized RMSE was recalculated for each case. The corresponding sensitivity results are presented in Section 3.

2.5.3. Energy Dissipation

The hysteretic energy dissipation was evaluated from the enclosed area of the experimental and numerical stress–strain loops using numerical integration. The same trapezoidal integration procedure was applied to the experimental data and to the numerical responses to ensure a consistent comparison. The energy density was calculated as

$$W = \int \sigma d\varepsilon \tag{11}$$

where the integration was performed numerically using the trapezoidal rule.

The global RMSE, localized plateau RMSE, and hysteretic energy dissipation were selected because they provide complementary information regarding the overall accuracy, transformation behavior, and energy absorption capability of the constitutive models.

3. Results

3.1. Test 1

In this section, the comparative performance of the Brinson and Liang–Rogers constitutive models is assessed against published experimental stress–strain data for the superelastic response measured at 65 °C [29]. The same loading history was applied to both models to enable a direct comparison of their predicted superelastic responses.

Figure 1 compares the stress–strain responses predicted by both models with the corresponding experimental data. Both models reproduce the main features of the superelastic cycle, which include the elastic region and forward and reverse transformation plateaus. These results indicate that, although both phenomenological models reproduce the overall superelastic stress–strain response, their agreement with the experimental response differs within the localized transformation plateau regions.

However, some notable differences are observed in the transformation plateau zone. The Liang–Rogers model shows closer agreement with the experimental upper transformation plateau, especially regarding the transition slope and stress evolution during transformation. On the other hand, the Brinson model predicts the response in a smoother transition. This difference may be attributed to the different constitutive descriptions of the stress-induced phase transformation adopted by the two models.

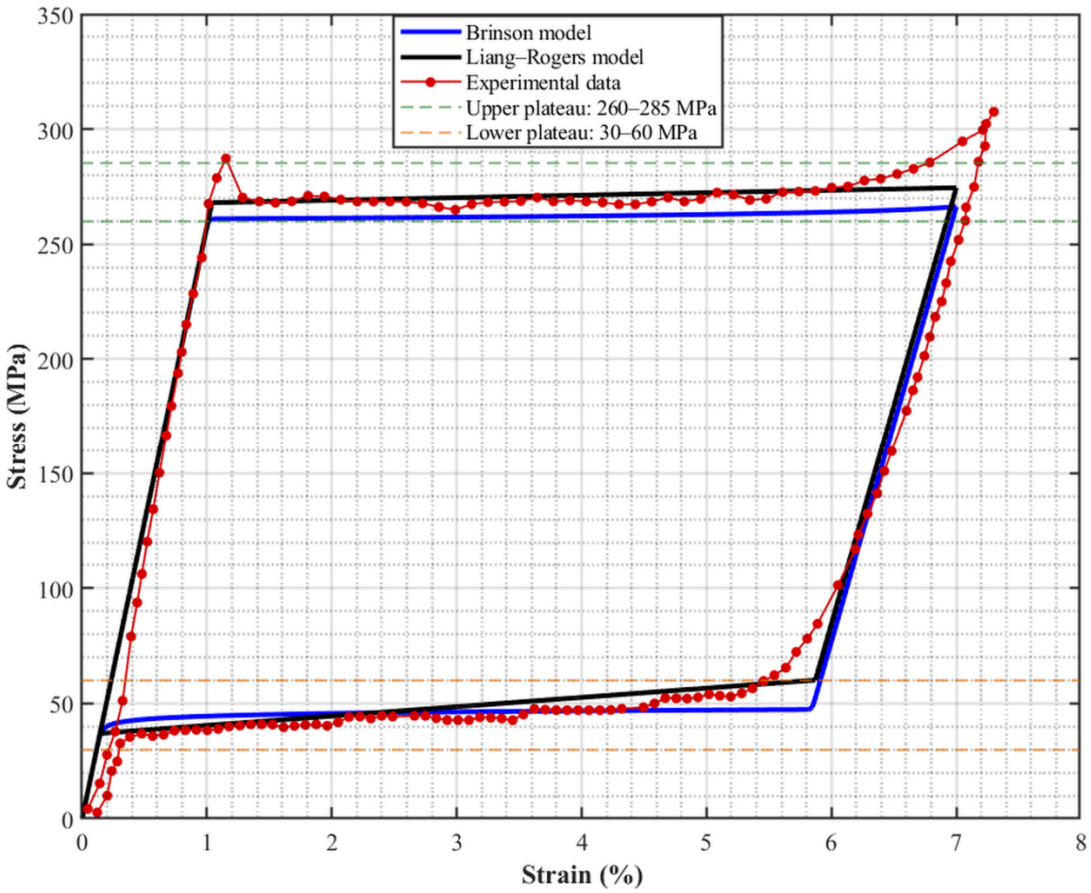


Figure 1. Comparison of experimental and numerical stress–strain responses predicted by the Brinson and Liang–Rogers constitutive models for Test 1.

Regarding the lower transformation plateau, both models exhibit similar stress evolution. Nevertheless, some deviations from the experimental response can still be noticed. During unloading, the Liang–Rogers model predicts a transformation that is steeper than that predicted by the Brinson model.

However, for higher strains, both models slightly underpredict the experimental results. Despite that, the Liang–Rogers formulation demonstrates closer agreement with the experimental hysteresis response, particularly at the localized transformation plateaus. These results indicate that, although both phenomenological models are able to capture the overall behavior of superelastic SMAs, significant differences exist in their localized transformation behavior.

3.1.1. Global RMSE

To quantitatively compare the agreement of the constitutive models with the experimental data, the root mean square error in Equation (9) is used.

The quantitative comparison of the two constitutive models based on the global RMSE and localized plateau RMSE is summarized in Table 4. As shown in Table 4, both constitutive models provide comparable agreement with the overall superelastic hysteresis response. Even though the Liang–Rogers model yields slightly smaller RMSE values, their difference is still rather modest when only the global RMSE is considered.

These results suggest that global RMSE-based comparison may lack the sensitivity required to assess the localized behavior of transformation processes. Consequently, additional localized error analysis is useful for distinguishing the comparative performance of the constitutive models in the transformation regions.

Table 4. Quantitative comparison of the Brinson and Liang–Rogers models for both comparative test cases.

Test Case	Model	Global RMSE (MPa)	Upper Plateau RMSE (MPa)	Lower Plateau RMSE (MPa)
Test 1	Brinson	11.99	8.78	7.47
	Liang–Rogers	11.69	3.46	4.85
Test 2	Brinson	25.41	11.51	10.35
	Liang–Rogers	23.89	7.69	7.49

3.1.2. Plateau RMSE

Apart from the global RMSE analysis, a localized error analysis was performed within the transformation plateau regions. This analysis was necessary because the transformation plateaus are critical regions of the superelastic hysteresis curve, as they correspond to the forward and reverse stress-induced martensitic transformations. In other words, the errors within such regions may be underrepresented when only global error metrics are applied.

The plateau boundaries defined in Section 2.5 were applied for the localized RMSE evaluation. The RMSE formulation used before was applied to analyze the errors in such regions.

Figure 2 presents a comparison of the localized RMSE values calculated for the upper and lower transformation plateaus. A clear difference in the comparative agreement of the two constitutive models with the experimental response is observed for the upper transformation plateau. As shown in Figure 2, the Liang–Rogers model yields substantially lower RMSE values than the Brinson model, which indicates closer agreement with the experimental stress–strain response within the transformation plateau region. This difference may be attributed to the different constitutive descriptions of the stress-induced phase transformation adopted by the two models, which result in different representations of the transformation plateau.

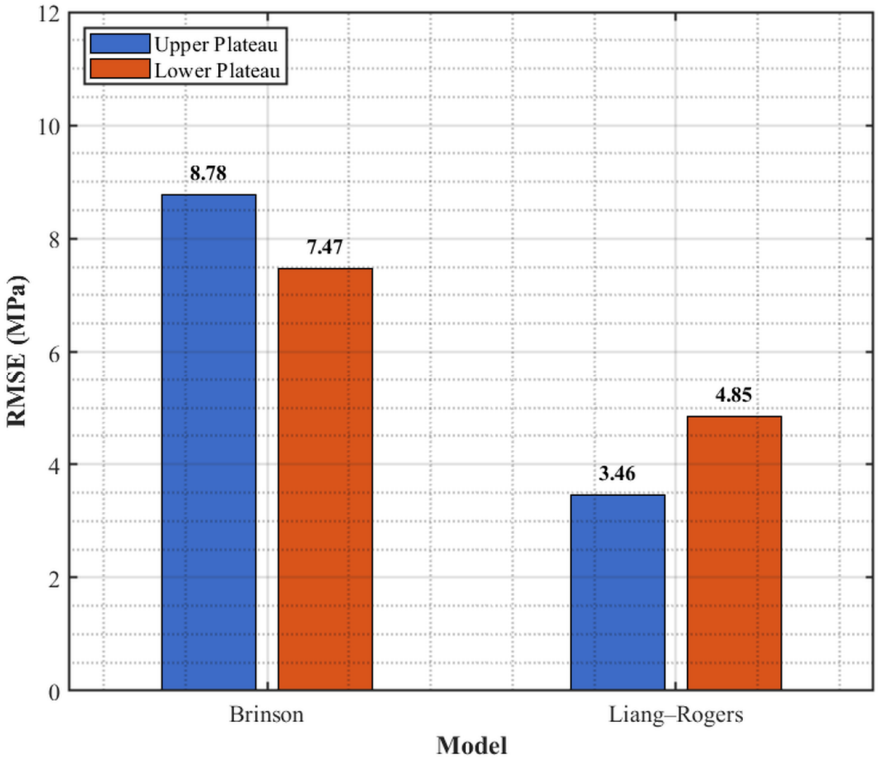


Figure 2. Comparison of localized plateau RMSE values for the Brinson and Liang–Rogers models (Test 1).

With respect to the lower transformation plateau, both models show good agreement with the experimental data. Nevertheless, the Liang–Rogers model continues to exhibit slightly lower RMSE values than the Brinson model, which indicates a modest improvement in localized agreement with the experimental response.

The above results indicate that, although both constitutive formulations provide comparable accuracy in reproducing the overall superelastic hysteresis response, localized plateau analysis enables a more discriminative comparison of their agreement with the experimental response.

Furthermore, the results suggest that differences in the constitutive formulation of the stress-induced phase transformation contribute to the observed differences in localized prediction accuracy.

3.1.3. Energy Dissipation

In addition to the stress–strain response, the hysteretic energy dissipation associated with the superelastic hysteresis loops was also investigated for the two formulations. For superelastic SMAs, the dissipated energy corresponds to the area bounded by the hysteresis loop and is an important parameter for evaluating damping capability and energy absorption performance.

For Test 1, the experimental hysteresis energy was 13.124 MJ/m^3, while the Brinson and Liang–Rogers models yielded 12.588 and 12.862 MJ/m^3, respectively. The corresponding relative deviations were 4.084% and 1.996%.

The results show that the hysteretic energy dissipation predicted by both constitutive models is close to the experimental value. The small difference between the predicted energy dissipation values shows that both constitutive models have comparable capability for representing the energy dissipation characteristics of the superelastic response.

This also reinforces the previously mentioned observation made based on the global RMSE analysis, i.e., the primary differences between the constitutive models occur at the local level of transformation.

To further examine whether these comparative trends remain consistent under different experimental conditions, a second comparative test case obtained from the same published experimental study was considered. The objective was to evaluate the consistency of the comparative trends observed in Test 1 under a different testing temperature. Therefore, the same comparative evaluation procedure, including global RMSE, localized plateau RMSE, and hysteretic energy dissipation, was applied to Test 2.

3.2. Test 2

The predicted stress–strain curves obtained using the Brinson and Liang–Rogers constitutive models for Test 2 at 70 °C [29] are compared with the experimental data in Figure 3. As observed for Test 1, both models reproduce the overall superelastic hysteresis response of NiTi SMA, including the elastic region, transformation plateaus, and reverse transformation during unloading.

As shown in Figure 3, both constitutive formulations provide good agreement with the overall stress–strain response. Nevertheless, differences between the model predictions and the experimental response can be observed for the transformation regions. Specifically, the Liang–Rogers model shows closer agreement with the transformation plateaus during loading and unloading.

During the loading stage, both constitutive models reproduce the upper transformation plateau. However, the Liang–Rogers model provides closer agreement with the experimental response throughout the transformation region. A similar trend is observed

during unloading, where the Liang–Rogers model also exhibits closer agreement with the experimentally observed reverse transformation plateau.

The quantitative performance metrics obtained for both tests are summarized in Table 4. Like in Test 1, the Liang–Rogers model provided lower global prediction errors while maintaining a closer agreement with the experimental stress–strain response.

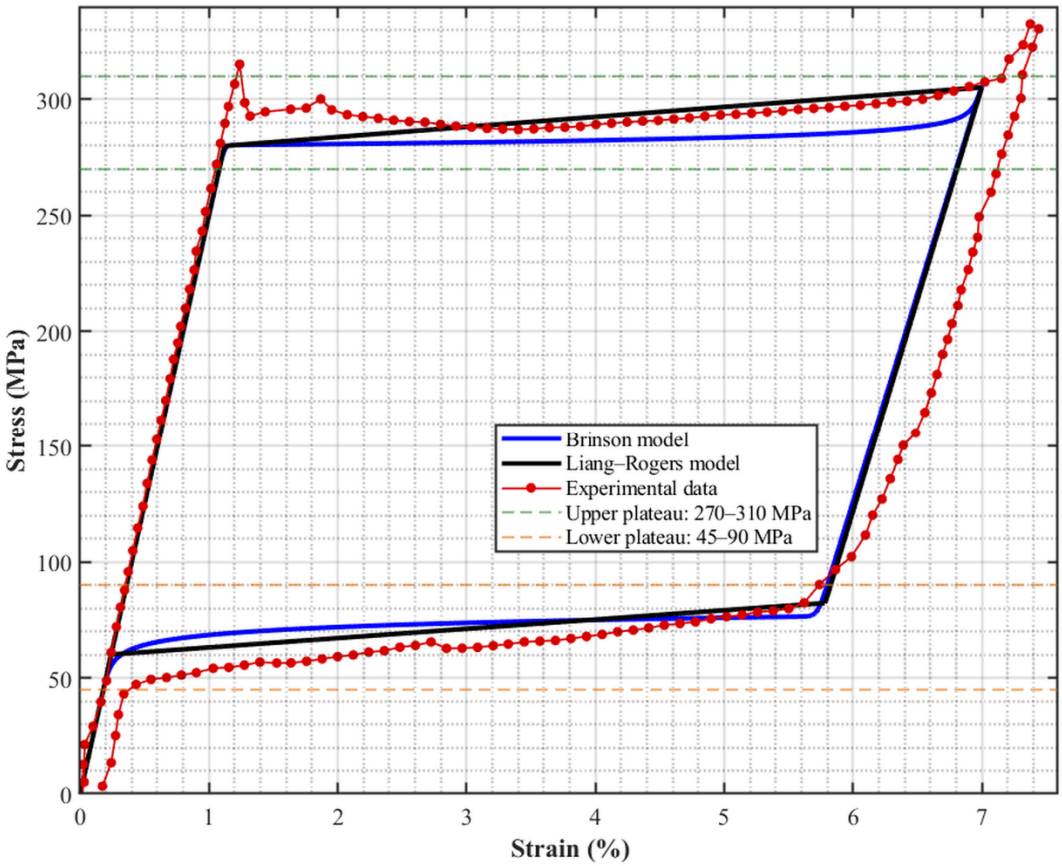


Figure 3. Comparison of experimental and numerical stress–strain responses predicted by the Brinson and Liang–Rogers constitutive models for Test 2.

The Liang–Rogers model yields a lower global RMSE for the loading–unloading cycle by approximately 6% compared to the Brinson model. While the reduction in the global RMSE remains relatively small, the obtained results are consistent with the observations from Test 1, in which the Liang–Rogers model showed marginally higher accuracy.

The localized plateau RMSE values presented in Table 4 and Figure 4 further confirm the superior agreement of the Liang–Rogers model within both the forward and reverse transformation regions.

These findings are consistent with those for Test 1. Although the global RMSE values provide relatively similar overall agreement, the localized plateau RMSE provides a more discriminative basis for comparing the agreement of the two constitutive models within the transformation regions.

Overall, the quantitative results consistently show that the Liang–Rogers model yields lower prediction errors than the Brinson model in both comparative test cases. Although the differences in global RMSE remain relatively small, the localized plateau analysis reveals a more pronounced distinction between the constitutive formulations, highlighting the importance of evaluating transformation regions in addition to global error metrics.

The sensitivity of the localized comparison to the selected plateau boundaries was also examined. As summarized in Table 5, the Liang–Rogers model consistently yielded

lower localized RMSE values than the Brinson model for both the upper and lower plateau regions across the narrowed, baseline, and widened boundary settings. This consistency indicates that the relative model ranking is not sensitive to reasonable variations in the selected plateau boundaries.

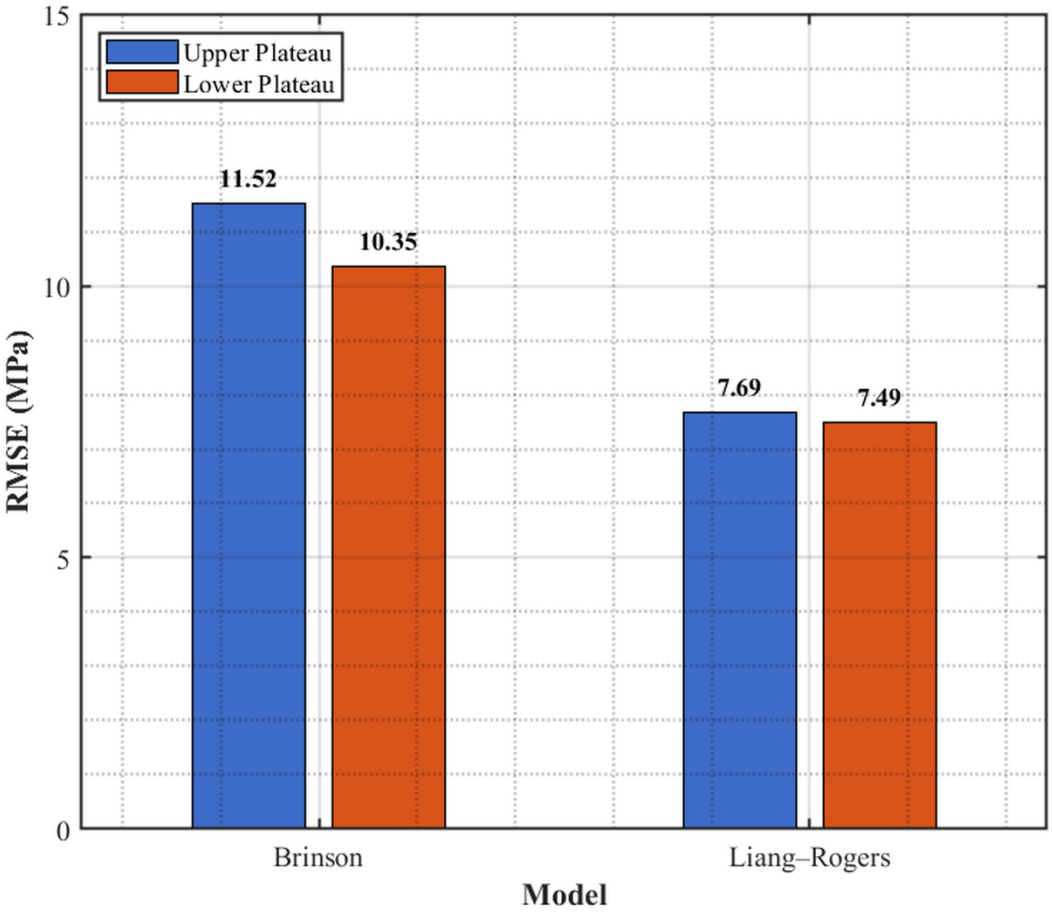


Figure 4. Comparison of localized plateau RMSE values for the Brinson and Liang–Rogers models (Test 2).

Table 5. Sensitivity of localized RMSE to variations in the selected plateau stress bounds.

Test	Plateau	Boundary Setting	Stress Interval (MPa)	Brinson RMSE (MPa)	Liang–Rogers RMSE (MPa)
Test 1	Upper	Narrowed	265–280	8.30	3.05
Test 1	Upper	Baseline	260–285	8.78	3.45
Test 1	Upper	Widened	255–290	9.86	4.69
Test 1	Lower	Narrowed	35–55	6.36	4.28
Test 1	Lower	Baseline	30–60	7.47	4.85
Test 1	Lower	Widened	25–65	8.25	5.49
Test 2	Upper	Narrowed	275–305	10.80	7.06
Test 2	Upper	Baseline	270–310	11.51	7.69
Test 2	Upper	Widened	265–315	11.51	7.69
Test 2	Lower	Narrowed	50–85	10.02	7.13
Test 2	Lower	Baseline	45–90	10.35	7.49
Test 2	Lower	Widened	40–95	10.55	7.85

The Liang–Rogers model consistently yielded a lower RMSE than the Brinson model for both the upper and lower plateau regions under all considered boundary settings,

which indicates that the relative model ranking was not sensitive to reasonable variations in the selected plateau boundaries.

To assess the robustness of the comparative results to moderate variations in the principal material parameters, a one-at-a-time sensitivity analysis was performed for the austenitic elastic modulus E_A, martensitic elastic modulus E_M, and maximum transformation strain ε_L, which directly characterize the elastic response and transformation strain of the SMA. Each parameter was independently varied by $\pm 5\%$ from its baseline value while the remaining parameters were kept unchanged, and the analysis was performed for both test conditions. The results are shown in Table 6.

Table 6. Sensitivity of global RMSE to $\pm 5\%$ variations in the principal material parameters.

Test	Parameter	Variation	Brinson RMSE (MPa)	Liang–Rogers RMSE (MPa)
Test 1	E_A	-5%	11.712	11.457
Test 1	E_A	0	11.998	11.694
Test 1	E_A	+5%	12.890	12.586
Test 1	E_M	-5%	11.903	11.694
Test 1	E_M	0	11.998	11.694
Test 1	E_M	+5%	12.214	11.694
Test 1	ε_L	-5%	12.099	11.868
Test 1	ε_L	0	11.998	11.694
Test 1	ε_L	+5%	12.049	11.583
Test 2	E_A	-5%	25.974	24.502
Test 2	E_A	0	25.416	23.891
Test 2	E_A	+5%	25.401	23.833
Test 2	E_M	-5%	24.242	23.891
Test 2	E_M	0	25.416	23.891
Test 2	E_M	+5%	31.096	23.891
Test 2	ε_L	-5%	45.564	24.537
Test 2	ε_L	0	25.416	23.891
Test 2	ε_L	+5%	23.328	19.932

The sensitivity analysis shows that the Liang–Rogers model consistently yields a lower global RMSE than the Brinson model for all considered variations of E_A, E_M, and ε_L in both test conditions. As expected from the constant austenitic modulus used in the Liang–Rogers formulation, variations in E_M do not affect its RMSE, whereas the Brinson model remains sensitive to E_M through its martensite-fraction-dependent effective modulus. Overall, these results indicate that the observed superior comparative performance of the Liang–Rogers formulation is maintained under moderate variations ($\pm 5\%$) in the principal material parameters.

To investigate the sensitivity of the comparative results to uncertainty associated with the extraction of the published experimental curves, a perturbation-based digitization uncertainty analysis was performed. Because the original raw experimental data were not available, a conservative stress perturbation of ± 2.5 MPa was applied to the extracted experimental stress values to represent a moderate level of graphical data-extraction uncertainty. The RMSE values were recalculated for both constitutive models under the positive and negative perturbations for both test conditions and are reported in Table 7.

The results demonstrate that the relative performance of the two constitutive models remains unchanged under the considered perturbations of the extracted experimental stress data. In all cases, the Liang–Rogers formulation yields a lower RMSE than the Brinson formulation, which indicates that the comparative results are robust with respect to the considered level of graphical data-extraction uncertainty.

Table 7. Sensitivity of the RMSE results to ±2.5 MPa perturbations of the extracted experimental stress data.

Test	Model	−2.5 MPa	Baseline	+2.5 MPa
Test 1	Brinson	12.368	11.998	12.143
Test 1	Liang–Rogers	10.945	11.694	10.753
Test 2	Brinson	26.384	25.416	24.664
Test 2	Liang–Rogers	25.005	23.891	22.996

Regarding hysteretic energy dissipation, the corresponding values for Test 2 were 13.539 MJ/m^3 for the experimental response, 11.917 MJ/m^3 for the Brinson model, and 12.400 MJ/m^3 for the Liang–Rogers model, corresponding to relative deviations of 11.984% and 8.416%, respectively. Detailed information, including the absolute and relative errors for each model, is reported in Table 8.

Table 8. Comparison of experimental and numerical hysteresis-loop energies for the two test cases. (All units are in $\left(\frac{\mathbf{MJ}}{\mathbf{m^3}}\right)$).

Test	Experimental Energy	Brinson Energy	Brinson Absolute Error	Brinson Relative Error	Liang–Rogers Energy	Liang–Rogers Absolute Error	Liang–Rogers Relative Error
Test 1	13.12	12.58	0.53	4.08	12.86	0.26	1.99
Test 2	13.54	11.91	1.62	11.98	12.40	1.14	8.41

The Liang–Rogers model therefore shows a lower deviation from the experimental hysteresis energy than the Brinson model for both test conditions.

4. Discussion

Comparison of the two test cases showed that both constitutive models reproduced the overall superelastic stress–strain response of the NiTi alloy under the investigated isothermal loading–unloading conditions. Specifically, the predicted stress–strain curves exhibited a characteristic hysteresis behavior featuring the elastic region, forward and reverse transformation plateaus, and recovery path. At the same time, noticeable differences become evident when the transformation regions were analyzed locally.

Consistent comparative trends were observed in both test cases conducted at 65 °C and 70 °C. In both Test 1 and Test 2, the Liang–Rogers model exhibited closer local agreement with the experimental stress–strain response within the transformation plateaus. In both comparative test cases, the difference in global agreement between the two models remained relatively small, however. Although the reduction in global RMSE was modest when global RMSE values were compared, a much more significant decrease was recorded for the plateau RMSE metric.

The obtained results also suggest that global error measures may not be sufficient as the sole criterion for constitutive model evaluation for superelastic SMAs. Although the global RMSE values of the two considered models were relatively close in both tests, localized plateau RMSE analysis revealed clear differences in localized agreement with the experimental response. As the transformation plateau regions are key features of the superelastic stress–strain response, localized error analysis can provide a more discriminative basis for model comparison than global RMSE alone. Relying solely on global RMSE may therefore overlook important differences in the agreement of the models within the transformation regions.

The observed differences between the two constitutive models are associated with their different constitutive treatments of the material response. Although both formulations employ cosine-based relations for the evolution of the martensitic fraction under the present

isothermal conditions, the Brinson formulation uses a martensite-fraction-dependent elastic modulus, whereas the Liang–Rogers formulation treats the elastic modulus as a constant material property. The temperature-induced martensite fraction in the Brinson formulation is zero under the present isothermal loading conditions and therefore does not constitute a source of difference between the two models in these comparative test cases. The different constitutive treatment of the elastic response contributes to the different stress representations observed within the transformation regions.

Conversely, the Liang–Rogers formulation yielded lower localized RMSE values within the transformation regions for both comparative test cases. This behavior indicates that, under the investigated loading conditions and parameter set, the Liang–Rogers constitutive treatment provides closer agreement with the experimentally observed transformation plateaus. Consequently, the Liang–Rogers model demonstrated closer local agreement with the experimental response while maintaining a comparable level of global agreement.

For both comparative cases, the two constitutive models predicted comparable hysteretic energy dissipation. This indicates that, despite the observed differences in localized transformation behavior, both formulations provide a similar representation of the overall energetic response associated with the superelastic hysteresis loop. Therefore, the localized differences identified by the plateau analysis do not necessarily translate into substantial differences in the predicted global energy dissipation.

According to the present results, within the investigated loading conditions, the selection of a constitutive model may depend on the intended engineering objective. When close representation of the experimental transformation plateaus is required, the Liang–Rogers model provides lower localized RMSE values under the investigated loading conditions. Conversely, the Brinson model provides comparable overall agreement with the experimental stress–strain response and hysteretic energy dissipation, which makes it a suitable alternative when global mechanical response is of primary interest. These findings are also relevant for numerical simulations of SMA-based smart structures, including aerospace applications, where accurate prediction of the transformation behavior is often required.

The present study is limited to two isothermal uniaxial tensile loading–unloading tests obtained from a single published experimental source. Therefore, the conclusions are restricted to the investigated loading conditions and should not be generalized to cyclic loading, non-isothermal behavior, multiaxial loading, or different SMA materials. Future studies should extend the proposed comparison framework to broader experimental datasets and more complex loading scenarios.

5. Conclusions

In this study, the comparative performance of the classical Brinson and Liang–Rogers one-dimensional phenomenological constitutive models was evaluated using two published experimental test cases corresponding to the superelastic response of NiTi shape memory alloys under isothermal tensile loading–unloading conditions at 65 and 70 °C.

The results demonstrate that both constitutive models reproduced the overall superelastic stress–strain response, including the loading path, transformation plateaus, unloading path, and hysteresis loop. Comparable global RMSE values and similar hysteretic energy dissipation were obtained, which indicates that both models provide comparable agreement with the global mechanical response under the investigated loading conditions.

The localized plateau analysis revealed that the Liang–Rogers model consistently produced lower RMSE values relative to the experimental response within the forward and reverse transformation regions for both test cases. The observed differences are associated with the different treatment of the constitutive response in the two formulations under

the investigated isothermal conditions. These results indicate that localized error metrics provide additional information beyond global RMSE and enable a more detailed assessment of constitutive model performance in the stress ranges where phase transformation predominantly occurs.

Although the Brinson model exhibited slightly higher localized prediction errors, it provided a comparable prediction of the overall stress–strain response and hysteretic energy dissipation. The present study demonstrates the usefulness of combining global and localized error metrics for the comparative assessment of constitutive models describing the superelastic behavior of shape memory alloys. The proposed plateau-based comparative evaluation framework provides a localized complement to conventional global error measures and may serve as a useful tool for future comparative studies involving constitutive model evaluation. Owing to the limited comparative scope considered in this work, the conclusions are restricted to the investigated isothermal loading conditions. Future research should extend the proposed methodology to independent experimental datasets, cyclic loading, non-isothermal conditions, and more complex thermomechanical loading paths relevant to SMA-based engineering applications, including aerospace structures.

Author Contributions: Conceptualization, editing, and supervision, G.C. and M.E.T.; conceptualization and writing—original draft, S.D.B. All authors have read and agreed to the published version of the manuscript.

Funding: This research received no external funding.

Data Availability Statement: The data that support the findings of this study are available from the corresponding author upon reasonable request.

Conflicts of Interest: The authors declare no conflicts of interest.

References

1. Ahmad, A.; Pranto, S.I.; Al Faruq, M.H.; Kasfia, M.T.T.; Rashid, A.B. A comprehensive overview of shape memory alloys: Recent advances in fabrications, properties, and applications for next-generation smart systems. *Next Mater.* **2026**, *10*, 101441. [CrossRef]
2. Jani, J.M.; Leary, M.; Subic, A.; Gibson, M.A. A review of shape memory alloy research, applications and opportunities. *Mater. Des.* **2014**, *56*, 1078–1113. [CrossRef]
3. Balasubramanian, M.; Srimath, R.; Vignesh, L.; Rajesh, S. Application of shape memory alloys in engineering, A review. *J. Phys. Conf. Ser.* **2021**, *2054*, 012078. [CrossRef]
4. Costanza, G.; Mercuri, S.; Porroni, I.; Tata, M.E. Shape Memory Alloys for Self-Centering Seismic Applications: A Review on Recent Advancements. *Machines* **2024**, *12*, 628. [CrossRef]
5. Rajan, C.; Latha, B. Smart Materials and Shape Memory Alloys for Aerospace Structures: Design, Actuation, and Fatigue Behavior. *Adv. Mech. Eng. Appl.* **2025**, *1*, 23–29.
6. Tandel, K.; Bhanumurthy, R.; Budarapu, P.R. Aeroelastic Stability Enhancement of Composite Laminates Using Embedded Pre-Strained NiTi Shape Memory Alloys. *Exp. Tech.* **2026**, *50*, 611–625. [CrossRef]
7. Kaur, H.; Thakur, A.K.; Gupta, L.R.; Dogra, S.; Singh, R. Advancements and Future Directions of Shape Memory Alloys in Aerospace Applications-A Comprehensive Review. *Evergreen* **2025**, *12*, 1484–1500. [CrossRef]
8. Alsawalhi, M.Y.; Landis, C.M. A new phenomenological constitutive model for shape memory alloys. *Int. J. Solids Struct.* **2022**, *257*, 111264. [CrossRef]
9. Kirsch, S.; Welsch, F.; Michaelis, N.; Schmidt, M.; Wieczorek, A.; Frenzel, J.; Eggeler, G.; Schütze, A.; Seelecke, S. NiTi-Based Elastocaloric Cooling on the Macroscale: From Basic Concepts to Realization. *Energy Technol.* **2018**, *6*, 1567. [CrossRef]
10. Song, Y.; He, Q.; Yam, M.C.H.; Zhao, Q.; Kim, K.S. Superelastic Behavior of Ni-Ti SMA Bars under Shear and Bending:Experiments, Modeling, and Application in Beam-to-Column Connections. *J. Struct. Eng.* **2025**, *151*, 7. [CrossRef]
11. Sun, Q.P.; Hwang, K.C. Micromechanics modelling for the constitutive behaviour of polycrystalline shape memory alloys. *J. Mech. Phys. Solids* **1993**, *41*, 1–17. [CrossRef]
12. Thamburaja, P. Constitutive equations for martensitic reorientation and detwinning in shape-memory alloys. *J. Mech. Phys. Solids* **2005**, *53*, 825–856. [CrossRef]
13. Cisse, C.; Zaki, W.; Ben Zineb, T. A review of constitutive models and modeling techniques for shape memory alloys. *Int. J. Plast.* **2016**, *76*, 244–284. [CrossRef]

14. Xu, L.; Solomou, A.; Baxevanis, T.; Lagoudas, D. Finite strain constitutive modeling for shape memory alloys considering transformation-induced plasticity and two-way shape memory effect. *Int. J. Solids Struct.* **2020**, *221*, 42–59. [CrossRef]
15. Morin, C.; Moumni, Z.; Zaki, W. A constitutive model for shape memory alloys accounting for thermomechanical coupling. *Int. J. Plast.* **2011**, *27*, 748–767. [CrossRef]
16. Boyd, J.G.; Lagoudas, D.C. A thermodynamic constitutive model for the shape memory materials part I. The monolithic shape memory alloys. *Int. J. Plast.* **1996**, *6*, 805–842. [CrossRef]
17. Brinson, L.C. One-dimensional constitutive behavior of shape memory alloys: Thermomechanical derivation with non-constant material functions and redefined martensite internal variable. *J. Intell. Mater. Syst. Struct.* **1993**, *4*, 229–242. [CrossRef]
18. Auricchio, F.; Reali, A. A Phenomenological One-Dimensional Model Describing Stress-Induced Solid Phase Transformation with Permanent Inelasticity. *Mech. Adv. Mater. Struct.* **2007**, *14*, 43–55. [CrossRef]
19. Liang, C.; Rogers, C.A. One-dimensional thermomechanical constitutive relations for shape memory materials. *J. Intell. Mater. Syst. Struct.* **1990**, *1*, 207–234. [CrossRef]
20. Tanaka, K. A thermomechanical sketch of shape memory effect: One-dimensional tensile behavior. *Res. Mech.* **1986**, *18*, 251–263.
21. He, B.; Dong, X.; Nie, R.; Wang, Y.; Ao, S.; Wang, G. Comprehensive shape memory alloys constitutive models for engineering application. *Mater. Des.* **2023**, *225*, 111563. [CrossRef]
22. Xu, B.; Zhou, X.; Yu, C. A multiscale analytical model for superelastic deformation of gradient nano-grained Ni-Ti shape memory alloys. *Acta Mech. Sin.* **2025**, *41*, 124342. [CrossRef]
23. Junker, P.; Hackl, K.A. Thermo-mechanically coupled field model for shape memory alloys. *Contin. Mech. Thermodyn.* **2014**, *26*, 859–877. [CrossRef]
24. Kundu, A.; Banerjee, A. Coupled thermomechanical modeling of shape memory alloy structures undergoing large deformation. *Int. J. Mech. Sci.* **2022**, *220*, 107102. [CrossRef]
25. Khandelwal, A.; Buravalla, V. Models for Shape Memory Alloy Behavior: An overview of modeling approaches. *Int. J. Struct. Changes Solids–Mech. Appl.* **2009**, *1*, 111–148.
26. Costanza, G.; Tata, M.E.; Danaee Barforooshi, S. Phenomenological Modeling of Shape Memory Alloys: A Review of Macroscopic Approaches. *Micromachines* **2025**, *16*, 1300. [CrossRef] [PubMed]
27. Prahlad, H.; Chopra, I. Comparative Evaluation of Shape Memory Alloy Constitutive Models with Experimental Data. *J. Intell. Mater. Syst. Struct.* **2001**, *12*, 6. [CrossRef]
28. Sayyaadi, H.; Zakerzadeh, M.R.; Salehi, H. A comparative analysis of some one-dimensional shape memory alloy constitutive models based on experimental tests. *Sci. Iran.* **2012**, *19*, 249–257. [CrossRef]
29. Zidane, I.; Meddour, B. On modelling of the one dimensional pseudoelastic effect of shape memory alloys. *Mech. Ind.* **2025**, *26*, 6. [CrossRef]
30. Ng, K.L.; Sun, Q.P. Stress-induced phase transformation and detwinning in NiTi polycrystalline shape memory alloy tubes. *Mech. Mater.* **2006**, *38*, 41–56. [CrossRef]

Disclaimer/Publisher's Note: The statements, opinions and data contained in all publications are solely those of the individual author(s) and contributor(s) and not of MDPI and/or the editor(s). MDPI and/or the editor(s) disclaim responsibility for any injury to people or property resulting from any ideas, methods, instructions or products referred to in the content.